# Effects of Hydrostatic Pressure and Uniaxial Strain on Spin-Peierls Transition in an Organic Radical Magnet, BBDTA·$InCl_4$

Masaki MITO*, Seiichiro KAWAGOE, Hiroyuki DEGUCHI, Seishi TAKAGI, Wataru FUJITA[1], Kunio AWAGA[2], Ryusuke KONDO[3], and Seiichi KAGOSHIMA[3]

*Faculty of Engineering, Kyushu Institute of Technology, Kitakyushu 804-8550, Japan*
[1]*Department of Chemistry, Tokyo Metroplitan University, Hachioji, Tokyo 192-0397, Japan*
[2]*Research Center for Materials Science, Nagoya University, Chikusa-ku, Nagoya 464-8602, Japan*
[3]*Department of Basic Science, the University of Tokyo, Meguro 3-8-1, Tokyo 152-8902, Japan*

We investigated the effects of hydrostatic pressure and uniaxial strain on the spin-Peierls (SP) transition of an organic radical magnet, benzo[1,2-d:4,5-d']bis[1,3,2]dithiazole(BBDTA)·$InCl_4$. It has a one-dimensional coordination polymer structure along its $c$-axis and its SP transition occurs at 108 K. The SP transition temperature $T_{SP}$ decreased to 99 K at a hydrostatic pressure of 10 kbar, while it increased to 132 K at a uniaxial strain along the $c$-axis of 8 kbar. The pressure dependences of $T_{SP}$ under these two conditions were discussed by evaluating two parameters, namely, the intrachain interaction $2J/k_B$ and the effective spin-lattice coupling parameter $\eta$, that are related to $T_{SP}$ by the equation $T_{SP} = 1.6\ \eta\ J/k_B$. Under ambient pressure, the $a$- and $c$-axes of this material shortened monotonically with decreasing temperature, while the $b$-axis elongated below $T_{SP}$. In this study, we found the correlation between $\eta$ and the change in the lattice constant $b$. $2J/k_B$ increased with increasing hydrostatic pressure and uniaxial strain, suggesting that the contraction along the $c$-axis does not depend on the manner of pressurization. From the evaluation of $\eta$, the observed variation in $T_{SP}$ is explained by the difference between the changes in $b$ under the two pressurization conditions.

KEYWORDS: Spin-Peierls transition, hydrostatic pressure, uniaxial strain, organic radical magnet

## 1. Introduction

The spin-Peierls (SP) transition is a magnetic-to-nonmagnetic transition accompanying structural transformation in a one-dimensional (1D) quantum spin system.[1)] Above the SP transition temperature ($T_{SP}$), there is a uniform 1D magnetic network, while bond alternation occurs below $T_{SP}$, resulting in an energy gap between the singlet ground state and the triplet excited state. In the SP transition, the energy gains due to this spin dimerization exceed the loss in elastic energy due to lattice distortion. Thus, an SP system is considered to be a spin

*E-mail: mitoh@tobata.isc.kyutech.ac.jp

system strongly coupled with a lattice. The Hamiltonian for the SP system is expressed as

$$\mathcal{H} = 2J\sum_l (1+\lambda\frac{u_l - u_{l+1}}{2d})\boldsymbol{S}_l \cdot \boldsymbol{S}_{l+1} + \frac{K}{2}\sum_l (u_l - u_{l+1})^2, \quad (1)$$

where $J$ is the exchange interaction, $\boldsymbol{S_l}$ is the spin operator for spin $S$, $u_l$ is the coordinate of the spin, $d$ is the lattice spacing, $\lambda$ is the spin-lattice coupling, and $K$ is the elastic constant.[2–4] $T_{\mathrm{SP}}$ can be expressed in terms of the product of the magnitude of the exchange interaction, $J$, and the generalized spin-lattice coupling parameter $\eta$ as

$$T_{\mathrm{SP}} = \frac{1.6\eta J}{k_{\mathrm{B}}}, \quad (2)$$

where $\eta$ is a function of $\lambda$ and $K$.[5]

Model materials that form SP systems are mostly organic radical crystals with a 1D stacking structure of planar magnetic molecules, such as MEM(TCNQ)$_2$[6] and p-CyDOV.[7] In addition, there are several inorganic SP materials, including $CuGeO_3$.[8] Because the SP spin system is strongly coupled with its lattice, the effect of pressure is very interesting. The effects of applying hydrostatic pressure on an SP system have been investigated in many materials, including MEM(TCNQ)$_2$,[9–11] (TMTTF)$_2$PF$_6$,[12,13] Li(DMe-DCNQI)$_2$,[14] (TMTTF)$_2$AsF$_6$,[15] $CuGeO_3$,[16–18] and TiOCl.[19] The effects of uniaxial pressure have also been investigated in $CuGeO_3$.[20] Indeed, various pressure responses have been observed, including a pressure-induced phase transition to an antiferromagnetic ordering phase or a superconducting phase, as well as shifts in $T_{\mathrm{SP}}$. In particular, the organic SP transition often becomes unstable on pressurization, making it difficult to explain the pressure responses only by the change in the magnetic exchange interactions.

Recently, thiazyl radicals have attracted the attention of materials scientists, because they exhibit interesting properties such as magnetic ordering,[21–24] room-temperature magnetic bistability,[25] photoinduced phase transitions,[26] metallic conduction,[27] and negative magnetoresistance.[28] We focused on the monocationic dithiazolyl radical ($S = 1/2$) of benzo[1,2-d:4,5-d']bis[1,3,2]dithiazole (BBDTA)[29] whose molecular structure is depicted in Fig. 1(a). 1:1 salts of BBDTA$^+$ with the diamagnetic anion In$X_4$ ($X$ = Cl or Br), BBDTA·In$X_4$, have high SP transition temperatures: 108 K for $X$ = Cl[30] and 250 K for $X$ = Br.[31] The crystal structure of BBDTA·InCl$_4$ is shown in Fig. 1(b).[30] The BBDTA$^+$ radical cation is directly coordinated to the indium atom in the InCl$_4^-$ unit via the nitrogen atom in the SNS ring, forming a one-dimensional coordination polymer structure along the $c$-axis. In most organic SP materials, organic radical molecules with a planar structure are stacked in columns. By contrast, the structure of BBDTA·InCl$_4$ resembles that of the inorganic SP material $CuGeO_3$, whose magnetic species are linked by covalent bonds via oxygen atoms.

In this paper, we present the structural and magnetic properties of the SP material BBDTA·InCl$_4$ under hydrostatic pressure and a uniaxial strain created along the one-

dimensional magnetic network. We succeeded in controlling the stability of the SP transition by varying the direction of the contraction applied to the regular 1D spin chain. The stability of the SP phase in this material under two types of pressure is examined in terms of the contributions of $J$ and $\eta$.

## 2. Experimental Procedure

Crystals of the thiazyl organic radical salt benzo[1,2-d:4,5-d']is[1,3,2]dithiazole(BBDTA)·$InCl_4$ (chemical formula: $C_6H_2Cl_4InN_2S_4$), were prepared in accordance with a procedure described elsewhere.[30] This crystal belongs to the orthorhombic system and its space group at room temperature is $Cmcm$. The structural parameters at room temperature are $a = 13.924(8)$ Å, $b = 10.490(5)$ Å, $c = 9.040(4)$ Å, and $Z = 4$.[30]

DC susceptibility measurement was performed at a DC magnetic field ($H$) of 1 T using a superconducting quantum interference device (SQUID) magnetometer (Quantum Design, MPMS-5S), which also has an AC mode. Contraction was realized using a piston cylinder cell that could be inserted into the SQUID magnetometer. The cell, with an inner diameter of 3.0 mm, was designed to hold a sample of more than 50 mg and apply pressures of up to 10 kbar at the temperature of the liquid helium. The magnitude ($P$) of the created hydrostatic pressure and uniaxial strain were estimated from the shift in the superconducting transition temperature ($T_C$) of lead, located at the center of the sample chamber, by measuring AC susceptibility.[32] No signal of lead appears in the DC measurement using $H = 1$ T, since the DC field exceeds the superconducting critical field of lead. Prior to the actual measurement, background signals of the pressure cell without the BBDTA·$InCl_4$ sample were observed every 0.5 mm of shrinkage. After subtracting the appropriate background response from the observed SQUID response at each temperature, magnetization was estimated by fitting the residual SQUID response using an analytical equation.

In the experiment under hydrostatic pressure, a liquidlike pressure-transmitting medium, Apiezon J oil, was used. To ensure effective pressurization, the sample was held inside the Teflon cell with Apiezon J oil and a small amount of metallic superconducting lead. The composition of the prepared sample for the hydrostatic experiments was as follows: 69.8 mg of polycrystalline BBDTA·$InCl_4$, 16.2 mg of Apiezon J oil, and 4.0 mg of lead. On the other hand, in the uniaxial strain experiments, the sample was fixed in epoxy resin (Stycast 1266, Ablestick Japan Co., Ltd.) with a small amount of lead. When using Stycast 1266 as the strain medium, generally, the Poisson effect can be neglected,[33] i.e., it is reasonable to assume that the lattice constant along the direction perpendicular to the load is unchanged.[34] As mentioned above, the magnitude of the uniaxial strain was evaluated from the shift in the $T_C$ of lead, so that the marker of stress became the same as that under the hydrostatic condition. By contrast, in conventional uniaxial pressure experiments, elongation along directions perpendicular to the

load occurs. The composition of the prepared sample in the present uniaxial strain experiment was as follows: 49.8 mg of regularly arrayed single crystals of BBDTA·$InCl_4$, 4.0 mg of lead, and sufficient Stycast 1266 to occupy the void space. The $c$-axis was perpendicular to the parallelogram plane of a single crystal. In the sample preparation for the uniaxial strain experiment, many single crystals were arranged on both sides of the plastic sheet and the mass was fixed in solidified Stycast 1266.

To estimate the lattice distortion in BBDTA·$InCl_4$ at temperatures between 50 and 295 K, X-ray diffraction (XRD) analysis of a single crystal was carried out.[35] Furthermore, powder XRD pattern analysis was performed at hydrostatic pressures of up to 11.5 kbar at room temperature, using a synchrotron radiation XRD diffractometer with a cylindrical imaging plate at the Photon Factory (PF) of the Institute of Materials Structure Science, the High Energy Accelerator Research Organization (KEK).[36] Pressure was applied with a diamond-anvil cell, which consists of diamonds with flat tips with a diameter of 0.6 mm and a 0.2-mm-thick CuBe gasket. Pressure was calibrated by the ruby fluorescence method.[37] In the sample cavity (diameter: 0.2 mm), which was located at the center of the gasket, the powdered sample and a few ruby crystals were inserted with the aid of a pressure-transmitting medium, fluorinated oil (FC77, Sumitomo 3M Co., Ltd.). The lattice parameters under pressure were determined on the basis of the peak angles of a series of diffraction patterns.

## 3. Experimental Results

### *3.1 Magnetic measurement under hydrostatic pressure*

Figure 2(a) shows the temperature dependence of the DC magnetic susceptibility $\chi = M/H$ at $H = 1$ T at $P \leq 9.7$ kbar. At ambient pressure, a broad hump due to the one-dimensional Heisenberg antiferromagnetic (1DHAF) correlation appeared over a wide temperature range above 110 K. In the high-temperature region, $\chi$ decreased rapidly below the characteristic temperature $T_{\rm SP}$, indicating the existence of a nonmagnetic state below $T_{\rm SP}$. Indeed, it is not easy to determine $T_{\rm SP}$ precisely in a series of pressure experiments. Herein, we estimated $T_{\rm SP}$ as the intersection point between the linear approximation of the data below $T_{\rm SP}$ and the theoretical curve of a 1DHAF system with $S = 1/2$ above $T_{\rm SP}$. On the low-temperature side, $\chi$ increased owing to the inevitable presence of a few percent of paramagnetic impurities. This characteristic persisted even at high pressures.

The experimental data after subtracting the impurity contribution are shown in Fig. 2(b). The solid curves (A) and (B) show the theoretical curves of the 1DHAF system at $P = 0$ and 6.5 kbar, respectively. For instance, $T_{\rm SP}$ at ambient pressure is indicated by the arrow and it was estimated to be 110 K. The values of $T_{\rm SP}$ at $P = 3.8$ and 6.5 kbar are 104 and 100 K, respectively. A pressure dependence series is shown in the inset of Fig. 2(B). The slope of the reduction in $T_{\rm SP}$ changes at about 1.3 kbar, and on both sides of this point the reduction varies linearly with pressure. The broad hump due to the 1DHAF correlation

shifted toward higher temperatures, accompanying the reduction in the magnitude of $\chi$. This indicates that the intensity of the antiferromagnetic exchange interaction increased when pressure was applied. $2J/k_{\rm B}$ was estimated by reproducing the broad hump, in the data from which the extrinsic paramagnetic contribution was subtracted, using the theoretical solution of the 1DHAF system.[38] The change in $2J/k_{\rm B}$ reflects the shift in the peak position ($T_{\rm max}$) as well as the change in the magnitude of $\chi$. The estimated values of $2J/k_{\rm B}$ at $P = 0$, 3.8, and 6.5 kbar were 280 ± 4 K ((A) in Fig. 2(b)), 289 ± 4 K, and 303 ± 4 K ((B) in Fig. 2(b)), respectively. $2J/k_{\rm B}$ at $P = 0$ kbar is sufficiently close to the value (277 K) in ref. 30. The pressure dependence of $2J/k_{\rm B}$ is shown in detail in Fig. 6(b). The slope changes at a pressure of about 1.3 kbar, similarly to the variation in $T_{\rm SP}$.

### *3.2 Magnetic measurement under uniaxial strain*

Figure 3(a) shows the $\chi(T)$ values when uniaxial strain was applied along the $c$-axis at $P_c = 0$, 2.5, and 7.5 kbar, which were estimated from the $T_{\rm C}$ of lead. The result at ambient pressure was consistent with that under hydrostatic pressure, except for a slight increase in the magnitude of $\chi$. The data after subtracting the paramagnetic contribution are shown in Fig. 3(b).

The inset of Fig. 3(b) shows the pressure dependence of $T_{\rm SP}$ when $T_{\rm SP}$ was estimated by a method similar to the method described in § 3.1. The pressure response at $T_{\rm SP}$ under uniaxial strain along the $c$-axis completely differed from that observed under the hydrostatic condition. At $P_c = 7.5$ kbar, there was a 19% increase in $T_{\rm SP}$.

In the pressure response of the broad hump due to the 1DHAF correlation, shifts toward the higher-temperature side are observed, accompanied by a reduction in the magnitude of $\chi$. To reproduce $\chi(T)$ at $P_c = 2.5$ and 7.5 kbar, it was necessary to adjust the number of spins ($N$) as well as $2J/k_{\rm B}$. Here, the parameter $2J/k_{\rm B}$ was used to adjust the peak position rather than the magnitude of $\chi$, while $N$ was adjusted so that the magnitude of $\chi$ in the theoretical solution became equal to the experimentally measured value. The estimated values of $2J/k_{\rm B}$ were 260 ± 4 K, 271 ± 4 K, and 284 ± 4 K at $P_c = 0$, 2.5, and 7.5 kbar, respectively. The change in $2J/k_{\rm B}$ is expressed by $2J/k_{\rm B}$ [K] = 261.3 + 3.1 × $P_c$ [kbar]. At $P_c = 7.5$ kbar, $2J/k_{\rm B}$ increased by 9.2% relative to its value at $P_c = 0$ kbar. A detailed comparison with the results under hydrostatic pressure is shown in Fig. 6(b). The rate of increase in $2J/k_{\rm B}$ appears to be independent of the form of pressure applied at $P$ (or $P_c$) ≥ 1.3 kbar, where a similar shrinkage along the $c$-axis is expected under both pressurization conditions. We obtained $N(P_c = 2.5$ kbar) = 0.97 $N(P_c = 0$ kbar) and $N(P_c = 7.5$ kbar) = 0.90 $N(P_c = 0$ kbar). The latter suggests that about 10% of the spin was released magnetically from the antiferromagnetic network, and that the spins may behave as paramagnetic spins at the ends of the magnetic chain. The enhancement in the paramagnetic contribution at temperatures below $T_{\rm SP}$ reflects the above phenomenon (see Fig. 3(a)).

### *3.3 XRD analysis*

#### *3.3.1 Temperature dependence of the lattice constants at ambient pressure*

Figure 4(a) shows the change in the lattice parameters as a function of temperature at ambient pressure, where each parameter was normalized using its value at 295 K. The structural distortion below $T_{SP}$ exhibited an anisotropic structural change. Specifically, when the temperature decreased below $T_{SP}$, both $a$ and $c$ continued to decrease, whereas $b$ commenced increasing at $T_{SP}$. The ratio $b/c$ decreased with decreasing temperature, and had a maximum near $T_{SP}$. These temperature dependences of the structural parameters reflect the lattice distortion at $T_{SP}$. Above $T_{SP}$, $BBDTA^+$ cations are located exactly halfway between the two $InCl_4^-$ units, forming a one-dimensional regular array of radical cations in the polymer chain, as shown in Fig. 4(b). Below $T_{SP}$, $BBDTA^+$ cations approach one side of the indium atoms on the $b$-axis, and the distance between $BBDTA^+$ cations alternates between long and short (see Fig. 4(c)). Such a structural change leads to the formation of a dimer, resulting in lattice elongation along the $b$-axis. This phenomenon has already been investigated in BBDTA·$InBr_4$ in detail.[31] The space group of BBDTA·$InCl_4$ at $T < T_{SP}$ is $Pmnm$, which is isostructural with BBDTA·$InBr_4$.[30]

#### *3.3.2 Powder XRD experiments under hydrostatic pressure at room temperature*

Figure 5(a) shows the powder XRD patterns of BBDTA·$InCl_4$ at room temperature when hydrostatic pressure was applied. The wavelength of the incident X-rays was 0.6834(1) Å. In this experiment, we investigated how the unit cell shrinks when hydrostatic pressure is applied. A long-time milling of the sample blurred the Debye-Scherrer rings. Therefore, milling time was restricted to a few minutes. Nevertheless, the Debye-Scherrer rings were not sufficiently sharp for the Rietveld analysis. We mainly monitored the position of a series of diffraction peaks to estimate the lattice parameters, after confirming that the space group did not change under pressure. The series of diffraction peaks was consistent with the simulation data based on the reported structure. Pressure was gradually increased from ambient pressure to 11.5 kbar, and the measurement was performed again at ambient pressure after releasing the pressure of 11.5 kbar. As well as the magnetic measurement data, these results confirm that the present crystal has sufficient elasticity against external stress.

Figure 5(b) shows the lattice parameters measured at each pressure, where each parameter was normalized using its initial value. Of the three principal axes, the $c$-axis exhibited the smallest shrinkage; this smallest shrinkage was evident at pressures below 2.5 kbar. On the other hand, in directions perpendicular to the $c$-axis (i.e., the $a$- and $b$-axes), linear shrinkage was observed over a wide pressure range. The slopes of the linear decay of the $a$, $b$, and $V$ normalized with respect to thier ambient pressure values were estimated to be $2.22 \times 10^{-3}$ $kbar^{-1}$, $1.44 \times 10^{-3}$ $kbar^{-1}$, and $4.96 \times 10^{-3}$ $kbar^{-1}$, respectively. At $P < 10$ kbar, $b/c$ became smaller than its value at ambient pressure. The shrinkage rate along the $b$-axis was

estimated to be about 1.4% at $P = 10$ kbar, where a volume shrinkage of about 5% occurred. The limited dependence of $2J/k_B$ on hydrostatic pressure at $P \leq 1.3$ kbar (see Fig. 6(b)), mentioned in § 3.1, may arise from the fact that the lattice constant of the $c$-axis hardly changes between 0 and 2.5 kbar.

## 4. Discussion

### *4.1 Comparison with other SP compounds*

Table I shows a summary of the pressure response of some prototypes of SP materials, which are compared with the result of BBDTA·$InCl_4$. To explain diverse pressure responses, physical factors except for $J$ and $\eta$ also have to be considered.

In MEM$(TCNQ)_2$ with $T_{SP} = 17$ K, the increase in $T_{SP}$ at pressures up to 2.8 kbar[9] and pressure-induced paramagnetism at pressures less than 1.0 kbar[10,11] may occur simultaneously under hydrostatic pressure. $(TMTTF)_2PF_6$ ($T_{SP} = 19$ K) enters the SP phase, the antiferromagnetic (AFM) ordering phase, the spin-density wave (SDW) phase, and finally the superconducting (SC) phase, as pressure is increased to 40 kbar.[12,13] As for Li$(DMe\text{-}DCNQI)_2$ ($T_{SP} = 80$ K), pressure-induced paramagnetism due to spin solitons caused by structural defects was observed.[14] $(TMTTF)_2AsF_6$ has charge ordering temperature of $T_{CO} = 103$ K and $T_{SP} = 11$ K (at $H = 9$ T). At pressures of up to 1.5 kbar, $T_{SP}$ increases substantially with increasing pressure, while $T_{CO}$ decreases rapidly. Charge ordering disappears at about $P =$ 1.5 kbar and $T_{SP}$ starts to drop.[15] Thus, the SP phase in the organic system often exhibits diverse responses under hydrostatic pressure.

In the inorganic SP compound $CuGeO_3$, the hydrostatic and uniaxial pressure dependences have been reported; the $T_{SP}$ of this material increases with increasing hydrostatic pressure.[16–18] Masuda *et al.* have observed the pressure-induced SP phase in highly Mg-doped $CuGeO_3$ with magnetic ordering.[39] This experiment suggests that, in the $CuGeO_3$ series, the magnetic competition between the nearest-neighbor intrachain interaction ($J_{NN}$) and the next nearest-neighbor one ($J_{NNN}$) along the $c$-axis stabilizes the SP phase, and that the effect of this competition overcomes the effect of the interchain interaction along the $a$- and $b$-axes under pressure. When the temperature is reduced below $T_{SP}$, the lattice constant $a$ commences increasing, the slope of the reduction in $b$ changes slightly and $c$ ceases to increase further. The uniaxial pressure acting toward the $a$-axis suppresses lattice elongation along the $a$-axis, reducing $T_{SP}$.[20] This quantitative pressure response $dT_{SP}/dP$ = -0.42 K/kbar is consistent with the estimate ($dT_{SP}/dP$ = -0.50 K/kbar) by Winkelmann *et al.* from the thermal expansion coefficients and the specific heat via the Ehrenfest relation.[40]

The hydrostatic pressure and uniaxial strain dependences of $T_{SP}$ and $2J/k_B$ for BBDTA·$InCl_4$ are summarized in Figs. 6(a) and 6(b), respectively. First, it is important to emphasize that $T_{SP}$ varies depending on whether the material shrinks hydrostatically or mainly along the $c$-axis. Next, the pressure dependences of $2J/k_B$ under the two conditions

are very similar: in both cases, $2J/k_B$ tends to increase with an increase in pressure. It is assumed that the contraction along the $c$-axis does not depend on the manner of pressurization. As shown in Table I, previous studies have shown that the organic SP phase often becomes unstable on pressurization.[10–15] The $dT_{SP}/dP$ for BBDTA·$InCl_4$ is also negative under hydrostatic pressure, whereas the sign of $dT_{SP}/dP$ becomes positive under uniaxial strain along the $c$-axis, despite the fact that $2J/k_B$ increases under both conditions. Thus, the pressure dependence of $T_{SP}$ for BBDTA·$InCl_4$ is not explainable only by the change in $2J/k_B$; the contribution of the coupling constant between the spin and lattice systems needs to be considered in addition to the variation in $2J/k_B$.

### *4.2 Structural interpretation for the pressure response of BBDTA·InCl$_4$*

Figure 6(c) shows the pressure dependence of $\eta$, estimated from eq. (2), for both hydrostatic pressure and uniaxial strain. $\eta$ decreases under hydrostatic pressure, whereas it increases under the uniaxial strain along the $c$-axis. The change in $\eta$ depends on the manner of pressurization. In this material, $\eta$ appears to be related to the deformation along the $b$-axis, which exhibits a characteristic temperature dependence below $T_{SP}$, as shown in Fig. 4(a). Under hydrostatic pressure, the SP transition is thought to be suppressed because elongation along the $b$-axis is restrained. Equation (2) indicates that when $\eta$ increases, the SP transition occurs at a higher temperature with greater extension along the $b$-axis. Hence, we are convinced that such a structural modification under hydrostatic pressure manifests itself as a reduction in $\eta$. We now attempt to deduce the structural modification of this material under uniaxial strain by considering $\eta$. Now we have no experimental data on lattice constants ($a$, $b$, and $c$) under the uniaxial strain, but we can suppose that the lattice constant $b$ hardly changes, relative to the variation in $c$. From the experimental viewpoint, it is true that the $b/c$ under the uniaxial strain along the $c$-axis is larger than that under hydrostatic pressure. Indeed under the uniaxial strain, $\eta$ slightly increases, as shown in Fig. 6(c). As a consequence, slight structural elongation along the $b$-axis might occur with the creation of uniaxial strain along the zigzag chain.

Here, we consider the effects of the interchain interaction on the decrease in $T_{SP}$ under the hydrostatic condition, accompanied by shrinkage along the interchain direction ($//a$, $b$) as well as that along the magnetic chain ($//c$), as shown in Fig. 5(b). Generally, the enhancement of the interchain interaction renders the SP phase unstable. From the present data, we were unable to find any distinct factor that induces a large change in the interchain interaction, such as the appearance of magnetic ordering. In fact, the target material exhibited a prominent lattice elongation along the $b$-axis at $T_{SP}$, and we assume that the pressure response of lattice elongation is more marked than the change in the interchain interaction.

The present target material BBDTA·$InCl_4$ exhibited no marked changes in its magnetic properties, such as the appearance of marked paramagnetic spin, or a transition to the SC

phase or AFM ordering phase. Rather, the 1D nature persisted throughout the pressure range considered; this is probably due to the coordination polymer structure. The pressure might function as an external source of perturbation to change both the magnetic coupling constant $2J/k_{\mathrm{B}}$ and the spin-lattice coupling constant $\eta$. Utilizing eq. (2) on the basis of the Hamiltonian of the SP system enabled quantitative analysis of $\eta$ as well as $2J/k_{\mathrm{B}}$ under both hydrostatic pressure and uniaxial strain. Similarly, it has been reported that uniaxial pressure noticeably modifies the magnetism of $CuGeO_3$.[16–18,20)]

## 5. Conclusion

We investigated the magnetic properties of the organic radical SP material BBDTA·$InCl_4$ using two different pressurizations. The exchange interaction was enhanced under both hydrostatic pressure and uniaxial strain along the magnetic chain direction ($c$-axis). It is suggested that the contraction along the $c$-axis does not depend on the manner of pressurization. However, the lattice elongation along the $b$-axis at the SP transition temperature ($T_{\mathrm{SP}}$) is affected by the manner of pressurization. Specifically, hydrostatic pressure suppressed the lattice elongation along the $b$-axis, whereas uniaxial strain induced no shrinkage along the $b$-axis. The difference in pressure response in $T_{\mathrm{SP}}$ is characterized by the variation in $b$. We clarified these experimental results for hydrostatic pressure and uniaxial strain by evaluating the magnetic exchange interaction and effective spin-lattice coupling parameter in the Hamiltonian of the SP system.

## Acknowledgment

This work was supported by a Grant-in-Aid for Scientific Research on Priority Areas, “ Application of Molecular Spins” (Area No. 769), from the Ministry of Education, Culture, Sports, Science and Technology (MEXT) of Japan.

## References


1) For review, see, J. W. Bray, L. V. Interrante, I. S. Jacobs, and J. C. Bonner: in *Extended Linear Chain Compounds*, ed. J. S. Miller (Plenum Press, London, 1983) Vol. 3.
2) S. Inagaki and H. Fukuyama: J. Phys. Soc. Jpn. **52** (1983) 2504.
3) S. Inagaki and H. Fukuyama: J. Phys. Soc. Jpn. **52** (1983) 3620.
4) H. Fukuyama, T. Tanimoto, and M. Saito: J. Phys. Soc. Jpn. **65** (1996) 1182.
5) M. C. Cross and D. S. Fisher: Phys. Rev. B **19** (1979) 402.
6) S. Huizinga, J. Kommandeur, G. A. Sawatzky, B. T. Thole, K. Kopinga, W. J. M. de Jonge, and J. Roos: Phys. Rev. B **19** (1979) 4723.
7) K. Mukai, N. Wada, J. B. Jamali, N. Achiwa, Y. Narumi, K. Kindo, T. Kobayashi, and K. Amaya: Chem. Phys. Lett. **257** (1996) 538.
8) See for example, M. Hase, I. Terasaki, and K. Uchinokura: Phys. Rev. Lett. **70** (1993) 3651.
9) D. Bloch, J. Voiron, C. Vettier, J. W. Bray, and S. Oostra: Physica B **119** (1983) 43.
10) S. Takagi, Y. Matsushita, Y. Yoshida, and H. Deguchi: Mol. Cryst. Liq. Cryst. **376** (2002) 377.
11) K. Ejima, T. Tajiri, H. Deguchi, M. Mito, S. Takagi, K. Owada, H. Nakao, and Y. Murakami: Physica B **329-333** (2003) 1195.
12) D. S. Chow, P. Wzietek, D. Fogliatti, B. Alavi, D. J. Tantillo, C. A. Merlic, and S. E. Brown: Phys. Rev. Lett. **81** (1998) 3984.
13) D. Jaccard, H. Wilhelm, D. Jerome, J. Moser, C. Carcel, and J. M. Fabre: J. Phys. Condens. Matter **13** (2001) L89.
14) M. Hiraoka, H. Sakamoto, K. Mizoguchi, and R. Kato: Phys. Rev. B **65** (2002) 174413.
15) F. Zamborszky, W. Yu, W. Raas, S. E. Brown, B. Alavi, C. A. Merlic, and A. Baur: Phys. Rev. B **66** (2002) 081103(R).
16) H. Takahashi, N. Mori, O. Fujita, J. Akimitsu, and T. Matsumoto: Solid State Commun. **95** (1995) 817.
17) M. Nishi, O. Fujita, J. Akimitsu, K. Kakurai, and Y. Fujii: Phys. Rev. B **52** (1995) R6959.
18) S. Katano, O. Fujita, J. Akimitsu, and M. Nishi: Phys. Rev. B **52** (1995) 15364.
19) S. Blanco-Canosa, F. Rivadulla, A. Pineiro, V. Pardo, D. Baldomir, D. I. Khomskii, M. M. Abd-Elmeguid, M. A. Lopez-Quintela, and J. Rivas: Phys. Rev. Lett. **102** (2009) 056406.
20) M. Nishi, J. Akimitsu, O. Fujita, K. Kakurai, and Y. Fujii: J. Phys. Soc. Jpn. **70**, Suppl. A. (2001) 172.
21) J. Banister, N. Bricklebank, I. Lavender, J. M. Rawson, C. I. Gregory, B. K. Tanner, W. Clegg, M. R. J. Elsegood, and F. Palacio: Angew. Chem. Int. Ed. Engl. **35** (1996) 2533.
22) C. M. Robertson, A. A. Leitch, K. Cvrkalj, R. W. Reed, D. J. T. Myles, P. A. Dube, and R. T. Oakley: J. Am. Chem. Soc. **130** (2008) 8414.
23) W. Fujita and K. Awaga: Chem. Phys. Lett. **388** (2004) 186.
24) W. Fujita and K. Kikuchi: Chem. Asian. J. **3** (2009) 400.
25) W. Fujita and K. Awaga: Science **286** (1999) 261.
26) H. Matsuzaki, W. Fujita, K. Awaga, and H. Okamoto: Phys. Rev. Lett. **91** (2003) 017403.
27) C.D. Bryan, A. W. Cordes, R. M. Fleming, N. A. George, S. H. Glarum, R. C. Haddon, R. T. Oakley, T. T. M. Palstra, A. S. Perel, L. F. Schneemeyer, and J. V. Waszczak: Nature **365** (1993) 821.

28) K. Okamoto, T. Tanaka, W. Fujita, K. Awaga, and T. Inabe: Angew. Chem. Int. Ed. **45** (2006) 4516.
29) T. M. Barclay, A. W. Cordes, R. H. de Laat, J. D. Goddard, R. C. Haddon, D. Y. Jeter, R. C. Mawhinney, R. T. Oakley, T. T. M. Palstra, G. W. Patenaude, R. W. Reed, and N. P. C. Westwood: J. Am. Chem. Soc. **119** (1997) 2633.
30) W. Fujita, K. Awaga, R. Kondo, and S. Kagoshima: J. Am. Chem. Soc. **128** (2006) 6016.
31) W. Fujita, K. Kikuchi, and K. Awaga: Angew. Chem. Int. Ed. **47** (2008) 9480.
32) A. Eiling and J. S. Schilling: J. Phys. F. **11** (1981) 623.
33) M. Maesato, Y. Koga, R. Kondo, and S. Kagoshima: Rev. Sci. Instrum. **71** (2000) 176.
34) F. Guo, K. Murata, A. Oda, Y. Mizuno, and H. Yoshino: J. Phys. Soc. Jpn. **69** (2000) 2164.
35) R. Kondo, S. Kagoshima, and J. Harada: Rev. Sci. Instrum. **76** (2005) 093902.
36) A. Fujiwara, K. Ishii, T. Watanuki, H. Suematsu, H. Nakao, K. Ohwada, Y. Fujii, Y. Murakami, T. Mori, H. Kawada, T. Kikegara, O. Shimomura, T. Matsubara, H. Hanabusa, S. Daicho, S. Kitamura, and C. Katayama: J. Appl. Cryst. **33** (2000) 1241.
37) G. J. Piermarini, S. Block, J. D. Barnett, and R. A. Forman: J. Appl. Phys. **46** (1975) 2774.
38) S. Eggert, I. Affleck, and M. Takahashi: Phys. Rev. Lett. **73** (1994) 332.
39) T. Masuda, D. Yano, R. Kuroda, K. Uchinokura, H. Kuroe, T. Sekine, Y. Katsuki, K. Ohwada, Y. Fujii, H. Nakao, and Y. Murakami: Phys. Rev. B **67** (2003) 024423.
40) H. Winkelmann, E. Gamper, B. Buchner, M. Braden, A. Revcolevschi, and G. Dhalenne: Phys. Rev. B **51** (1995) 12884.

Fig. 1. (a) Structure of the $BBDTA^+$ radical cation and (b) the crystal structure of $BBDTA{\cdot}InCl_4$ (molecular formula: $C_6H_2Cl_4InN_2S_4$) at room temperature. One $BBDTA^+$ radical cation possesses an unpaired electron, and the salt has a spin ($S$) of 1/2. This material has a 1D coordination polymer structure along the $c$-axis.

Fig. 2. (a) Temperature dependence of the DC magnetic susceptibility $\chi = M/H$ at $H = 1$ T ($\chi(T)$) and $P \leq 9.7$ kbar under the hydrostatic condition. The broken curve indicates the extrinsic paramagnetic contribution. (b) $\chi(T)$ after subtracting the paramagnetic contribution at $P = 0$, 3.8, and 6.5 kbar. The solid curves represent the theoretical solution of the $S = 1/2$ 1DHAF system at $2J/k_B =$ (A) 280 and (B) 303 K. $T_{SP}$ was determined from the intersection point between the above theoretical solution and the linear approximation on the low-temperature side. For instance, $T_{SP}$ at ambient pressure is indicated by the arrow. The inset of (b) shows the pressure dependence of $T_{SP}$ (the same data are also shown in Fig. 6(a)).

Fig. 3. (a) $\chi(T)$ for the uniaxial strain along the $c$-axis for $P_c = 0$, 2.5, and 7.5 kbar. The broken curve represents the extrinsic paramagnetic contribution. (b) $\chi(T)$ after subtracting the paramagnetic contribution. The solid curves represent the theoretical solution of the $S = 1/2$ 1DHAF system at $2J/k_B =$ (A) 260, (B) 271, and (C) 284 K. $T_{SP}$ was determined using a method similar to that mentioned in Fig. 2. The solid lines indicate the linear approximation of the rapid drop in $\chi$ at temperatures below $T_{SP}$ at each pressure. For instance, $T_{SP}$ at ambient pressure is indicated by an arrow. The inset of (b) shows the pressure dependence of $T_{SP}$ (the same data are also shown in Fig. 6(a)).

Fig. 4. (a) Temperature dependence of the three lattice parameters ($a$, $b$, $c$), $b/c$, and the unit cell volume ($V$) at ambient pressure. Each structural parameter is normalized using its value at 295 K. (b) Schematic presentation of the molecular alignment of $BBDTA^+$ cations along the $c$-axis in $BBDTA{\cdot}InCl_4$ at $T > T_{SP}$ and (c) $T \leq T_{SP}$. The intermolecular short contacts related to the dimerization are indicated by a bold broken line.

Fig. 5. (a) Powder XRD pattern at room temperature for hydrostatic pressures of up to 11.5 kbar. The series of diffraction peaks is labeled using the plane index of the orthorhombic symmetry. As a visual guide, the broken line indicates the peak position of the diffraction of the (111) plane in the initial state. (b) Pressure dependences of $a$, $b$, $c$, and $V$ under hydrostatic pressure. The lattice parameters were estimated by analyzing the peak position of the series of diffraction peaks in (a). Each parameter was normalized using its initial value. $a$, $b$, and $V$ were confirmed to have linear relationship with pressure; they had the following slopes: $2.22\times10^{-3}$ $kbar^{-1}$ for $a$, $1.44\times10^{-3}$ $kbar^{-1}$ for $b$, and $4.96\times10^{-3}$ $kbar^{-1}$ for $V$. $c$ hardly changed below 2.5 kbar, whereas at higher pressures it decreased linearly with pressure.

Fig. 6. Pressure dependences of (a) $T_{\rm SP}$, (b) $2J/k_{\rm B}$, and (c) generalized spin-lattice coupling constant, $\eta$, under both hydrostatic pressure (open circles) and the uniaxial strain along the $c$-axis (closed circles): $T_{\rm SP}$, $2J/k_{\rm B}$, and $\eta$ under the uniaxial strain have the following linear pressure dependences: $T_{\rm SP}$ [K] = 112.6 [K] + 3.0 [K/kbar] $\times$ $P_c$ [kbar], $2J/k_{\rm B}$ [K] = 261.3 [K] + 3.1 [K/kbar] $\times$ $P_c$ [kbar], and $\eta = 5.4 \times 10^{-1} + 5.6 \times 10^{-3}$ [/kbar] $\times$ $P_c$ [kbar], respectively. The other solid curves in the three figures serve as visual guides.

Table I. Pressure response of some SP materials. The "pressurization style" is selected among hydrostatic pressure (h-p), uniaxial pressure (u-p), and uniaxial strain (u-s). In the description of "pressure response", the following abbreviated words appear : spin-Peierls phase (SP), pressure-induced paramagnetism (PIP), antiferromagnetic ordering phase (AFM), spin density wave phase (SDW), and superconducting phase (SC). The symbols $\nearrow$ and $\searrow$ represent an increase and a decrease, respectively.

| | pressurization style | $T_{\rm SP}$ ($P = 0$) | pressure response | ref. |
|---|---|---|---|---|
| $MCM(TCNQ)_2$ | h-p | 17 K | $\nearrow$ in $T_{\rm SP}$ + PIP | 9-11 |
| $(TMTTF)_2PF_6$ | h-p | 19 K | SP $\rightarrow$ AFM $\rightarrow$ SDW $\rightarrow$ SC | 12, 13 |
| $Li(DMe\text{-}DCNQI)_2$ | h-p | 80 K | PIP | 14 |
| $(TMTTF)_2AsF_6$ | h-p | 11 K (9 T) | $\nearrow$ and $\searrow$ in $T_{\rm SP}$ | 15 |
| $CuGeO_3$ | h-p | 14 K | $\nearrow$ in $T_{\rm SP}$ | 16-18 |
| | u-p ($//a$) | | $\searrow$ in $T_{\rm SP}$ | 20 |
| $BBDTA{\cdot}InCl_4$ | h-p | 108 K | $\searrow$ in $T_{\rm SP}$ | present work |
| | u-s ($//c$) | | $\nearrow$ in $T_{\rm SP}$ | present work |

(a)

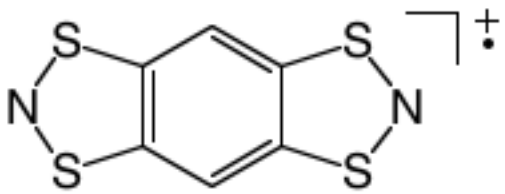


BBDTA$^+$
$S$ = 1/2

(b)

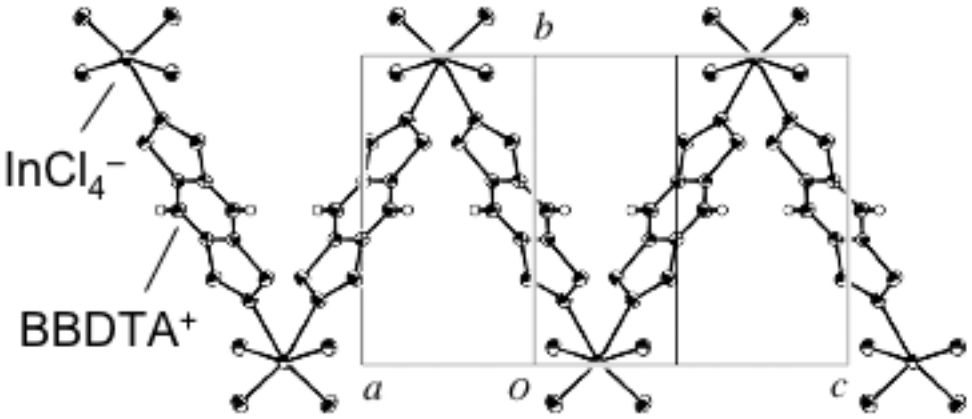


Fig. 1

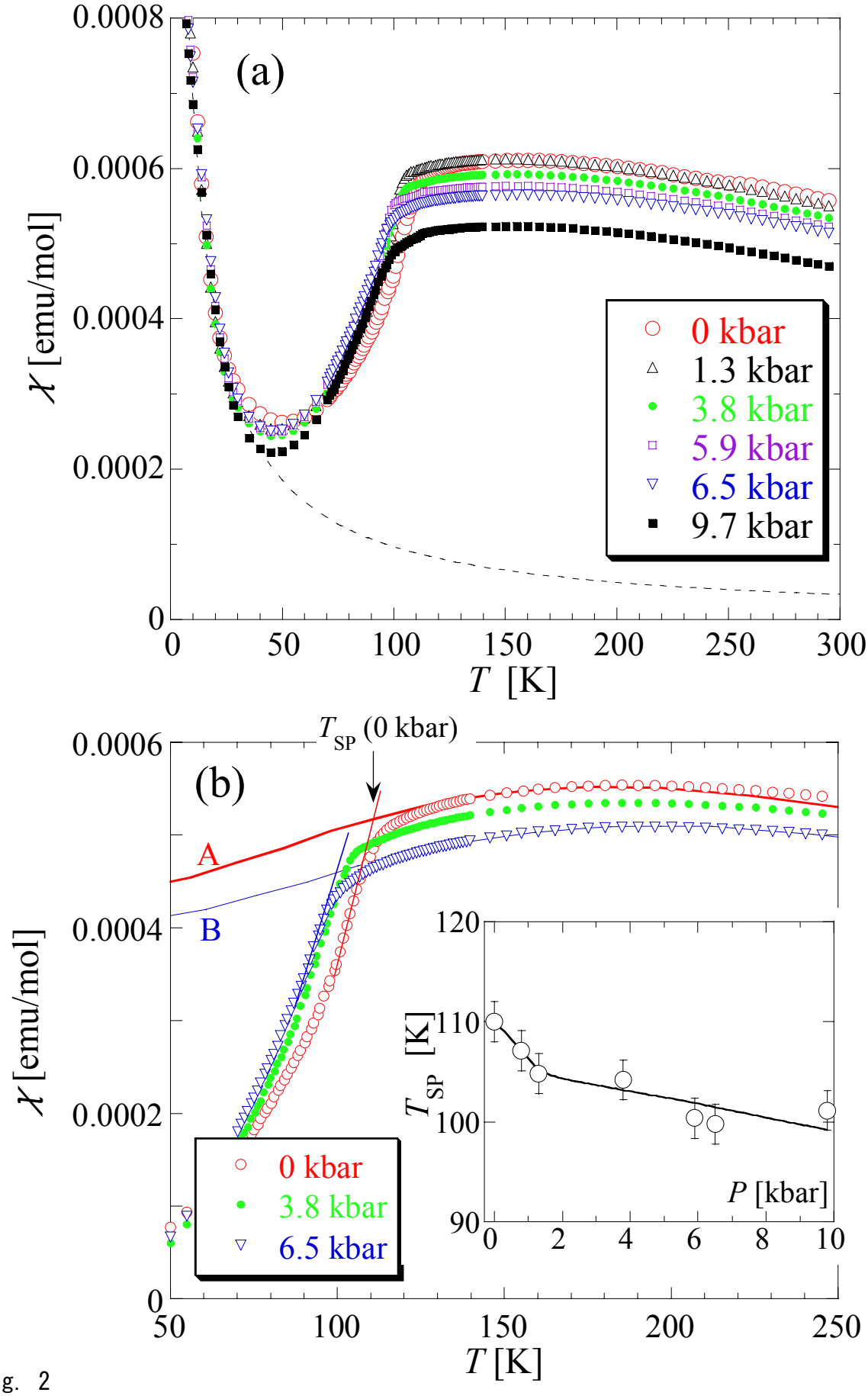
(a)
0.0008
0.0006
0.0004
0.0002
0
χ [emu/mol]
0
50
100
150
200
250
300
T [K]
0 kbar
1.3 kbar
3.8 kbar
5.9 kbar
6.5 kbar
9.7 kbar
(b)
T_SP (0 kbar)
A
B
0.0006
0.0004
0.0002
0
χ [emu/mol]
50
100
150
200
250
T [K]
0 kbar
3.8 kbar
6.5 kbar
120
110
100
90
T_SP [K]
0
2
4
6
8
10
P [kbar]

Fig. 2

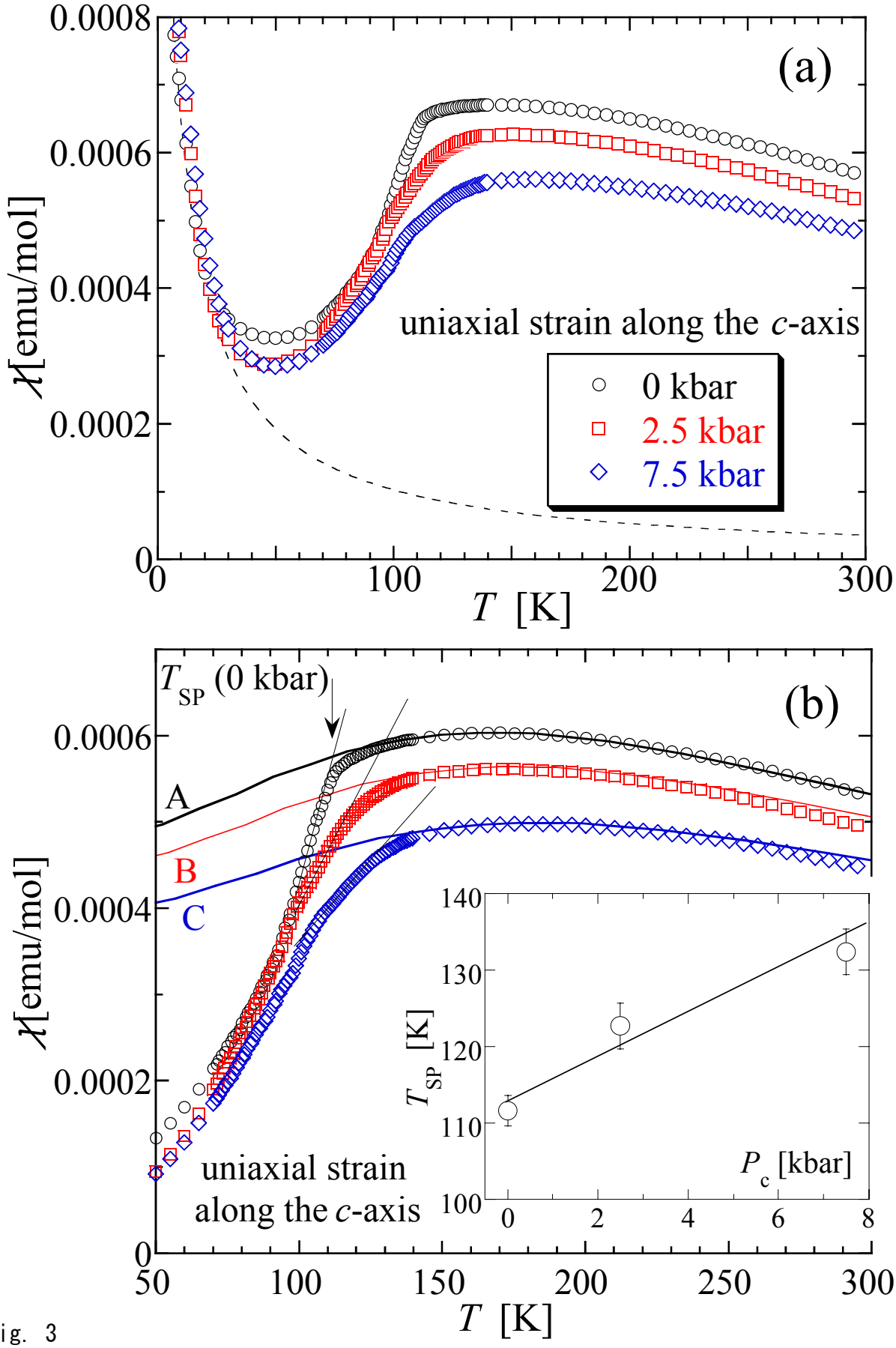
(a)
0.0008
0.0006
0.0004
0.0002
0
χ[emu/mol]
0
100
200
300
T [K]
uniaxial strain along the c-axis
0 kbar
2.5 kbar
7.5 kbar
(b)
T_SP (0 kbar)
A
B
C
0.0006
0.0004
0.0002
0
χ[emu/mol]
uniaxial strain
along the c-axis
140
130
120
110
100
T_SP [K]
P_c [kbar]
0
2
4
6
8
50
100
150
200
250
300
T [K]

Fig. 3

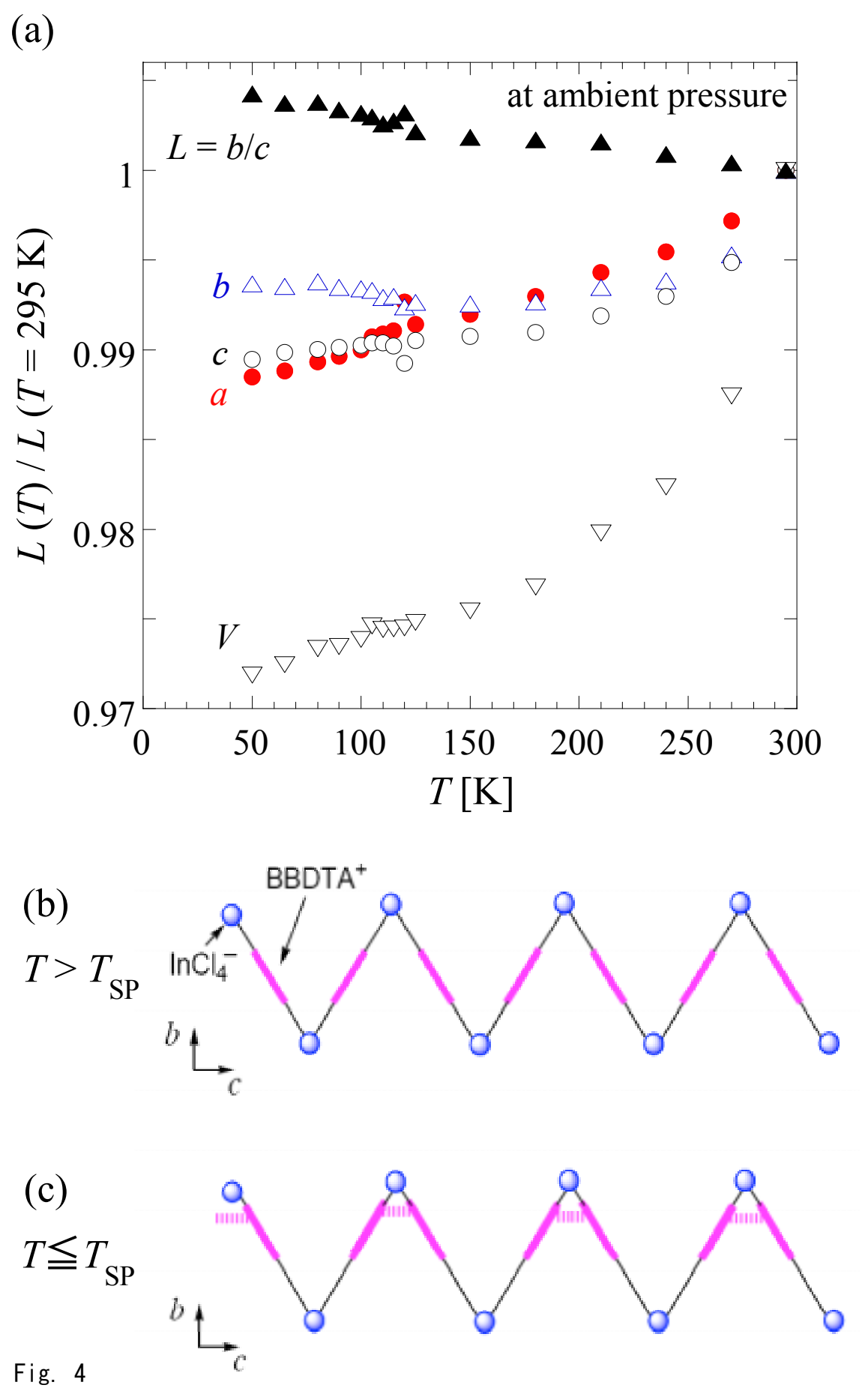
(a)
at ambient pressure
L = b/c
b
c
a
V
L (T) / L (T = 295 K)
1
0.99
0.98
0.97
0
50
100
150
200
250
300
T [K]
(b)
T > T_SP
BBDTA+
InCl4−
b
c
(c)
T ≦ T_SP
b
c

Fig. 4

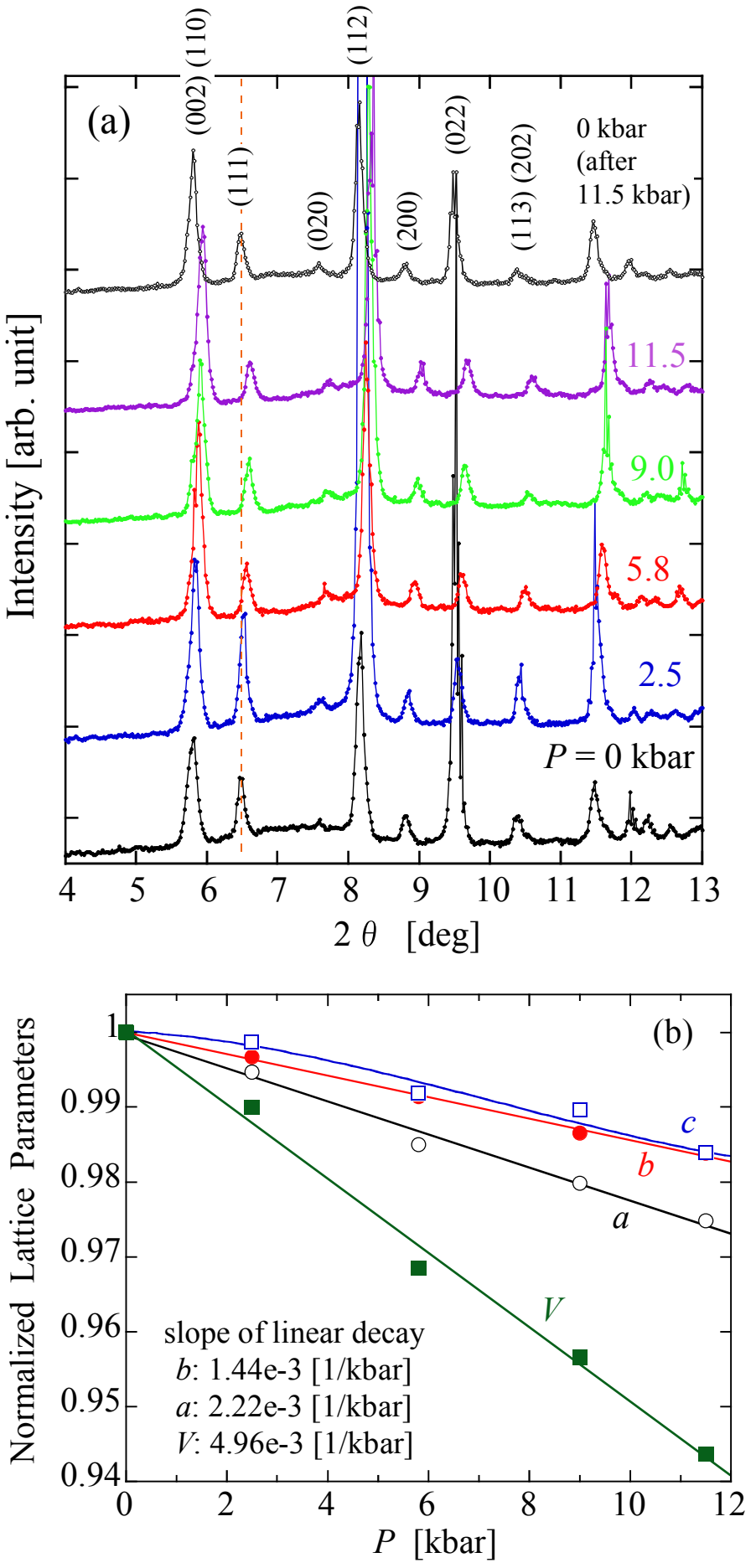
(a)
(002)
(110)
(111)
(020)
(112)
(200)
(022)
(113)
(202)
0 kbar
(after
11.5 kbar)
11.5
9.0
5.8
2.5
P = 0 kbar
Intensity [arb. unit]
2 θ [deg]
(b)
c
b
a
V
slope of linear decay
b: 1.44e-3 [1/kbar]
a: 2.22e-3 [1/kbar]
V: 4.96e-3 [1/kbar]
Normalized Lattice Parameters
P [kbar]

Fig. 5

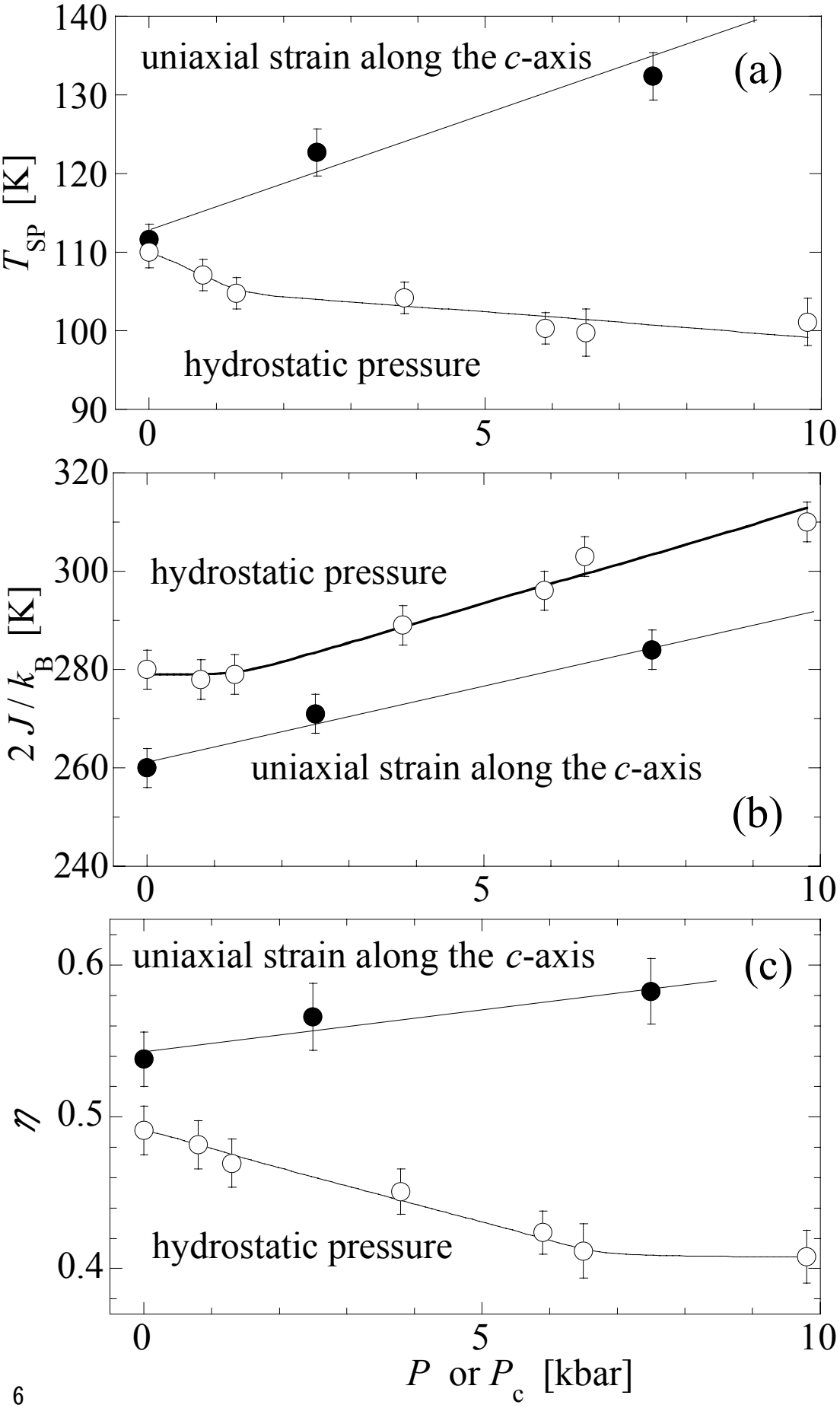
uniaxial strain along the c-axis
(a)
hydrostatic pressure
$T_{SP}$ [K]
140
130
120
110
100
90
0
5
10
hydrostatic pressure
uniaxial strain along the c-axis
(b)
$2J/k_B$ [K]
320
300
280
260
240
uniaxial strain along the c-axis
(c)
hydrostatic pressure
$\eta$
0.6
0.5
0.4
$P$ or $P_c$ [kbar]

Fig. 6